transcribed in developing endosperm (supplementary text). Peak transcript abundance coincides with the dramatic increase in linoleic acid content that occurs during seed development at the perisperm-endosperm transition (*27*).

Our analysis of the adaptive genomic landscape of *C. canephora* identifies the convergent evolution of caffeine biosynthesis among plant lineages and establishes coffee as a reference species for understanding the evolution of genome structure in asterid angiosperms.

REFERENCES AND NOTES

1. E. Robbrecht, J. F. Manen, *Syst. Geogr. Plants* **76**, 85–146 (2006).
2. P. Lashermes *et al*., *Mol. Gen. Genet.* **261**, 259–266 (1999).
3. M. Noirot *et al*., *Ann. Bot. (London)* **92**, 709–714 (2003).
4. Materials and methods are available as supplementary materials on *Science* Online.
5. S. Schaack, C. Gilbert, C. Feschotte, *Trends Ecol. Evol.* **25**, 537–546 (2010).
6. A. Roulin *et al*., *BMC Evol. Biol.* **9**, 58 (2009).
7. M. El Baidouri *et al*., *Genome Res.* **24**, 831–838 (2014).
8. C. Moisy, A. H. Schulman, R. Kalendar, J. P. Buchmann, F. Pelsy, *Theor. Appl. Genet.* **127**, 1223–1235 (2014).
9. O. Jaillon *et al*., *Nature* **449**, 463–467 (2007).
10. S. Sato *et al*., *Nature* **485**, 635–641 (2012).
11. P. Librado, F. G. Vieira, J. Rozas, *Bioinformatics* **28**, 279–281 (2012).
12. S. H. Hulbert, C. A. Webb, S. M. Smith, Q. Sun, *Annu. Rev. Phytopathol.* **39**, 285–312 (2001).
13. L. McHale, X. Tan, P. Koehl, R. W. Michelmore, *Genome Biol.* **7**, 212 (2006).
14. F. Gleason, R. Chollet, *Plant Biochemistry* (Jones and Bartlett, Sudbury, MA, 2011).
15. J. A. Nathanson, *Science* **226**, 184–187 (1984).
16. A. Pacheco, J. Pohlan, M. Schulz, *Allelopathy J.* **21**, 39–56 (2008).
17. H. Ashihara, H. Sano, A. Crozier, *Phytochemistry* **69**, 841–856 (2008).
18. A. A. McCarthy, J. G. McCarthy, *Plant Physiol.* **144**, 879–889 (2007).
19. M. Ogawa, Y. Herai, N. Koizumi, T. Kusano, H. Sano, *J. Biol. Chem.* **276**, 8213–8218 (2001).
20. E. Pichersky, E. Lewinsohn, *Annu. Rev. Plant Biol.* **62**, 549–566 (2011).
21. B. Field, A. E. Osbourn, *Science* **320**, 543–547 (2008).
22. M. Matsuno *et al*., *Science* **325**, 1688–1692 (2009).
23. B. Field *et al*., *Proc. Natl. Acad. Sci. U.S.A.* **108**, 16116–16121 (2011).
24. J. Zhang, R. Nielsen, Z. Yang, *Mol. Biol. Evol.* **22**, 2472–2479 (2005).
25. D. Villarreal *et al*., *J. Agric. Food Chem.* **57**, 11321–11327 (2009).
26. S. Dussert, A. Laffargue, A. de Kochko, T. Joët, *Phytochemistry* **69**, 2950–2960 (2008).
27. T. Joët *et al*., *New Phytol.* **182**, 146–162 (2009).

ACKNOWLEDGMENTS

We acknowledge the following sources for funding: ANR-08-GENM-022-001 (to P.L.); ANR-09-GENM-014-002 (to P.W.); Australian Research Council (to R.J.H.); Natural Sciences and Engineering Research Council of Canada (to D.S.); CNR-ENEA Agrifood Project A2 C44 L191 (to G.Gi.); FINEP-Qualicafé, INCT-CAFÉ (to A.C.A.); NSF grants 0922742 (to V.A.A.) and 0922545 (to R.M.); and the College of Arts and Sciences, University at Buffalo (to V.A.A.). We thank P. Facella (ENEA) for Roche 454 sequencing and Instituto Agronômico do Paraná (Paraná, Brazil) for fruit RNA. This work was supported by the high-performance cluster of the SouthGreen Bioinformatics platform (UMR AGAP) CIRAD (www.southgreen.fr). The *C. canephora* genome assembly and gene models are available on the Coffee Genome Hub (http://coffee-genome.org) and the CoGe platform (www.genomevolution.org). Sequencing data are deposited in the European Nucleotide Archive under the accession numbers CBUE020000001 to CBUE020025216 (contigs), HG739085 to HG752429 (scaffolds), and HG974428 to HG974439 (chromosomes). Gene family alignments and phylogenetic trees for BAHD acyltransferases and NMTs are available in the GreenPhylDB (www.greenphyl.org/cgi-bin/index.cgi) under the gene family IDs CF158535 and CF158539 to CF158545, respectively. We declare no competing financial interests.

SUPPLEMENTARY MATERIALS

www.sciencemag.org/content/345/6201/1181/suppl/DC1
Materials and Methods
Supplementary Text
Figs. S1 to S33
Tables S1 to S27
References (*28*–*175*)

28 April 2014; accepted 29 July 2014
10.1126/science.1255274

GENOME EDITING

Prevention of muscular dystrophy in mice by CRISPR/Cas9–mediated editing of germline DNA

Chengzu Long,[1]* John R. McAnally,[1]* John M. Shelton,[2] Alex A. Mireault,[1] Rhonda Bassel-Duby,[1] Eric N. Olson[1]†

Duchenne muscular dystrophy (DMD) is an inherited X-linked disease caused by mutations in the gene encoding dystrophin, a protein required for muscle fiber integrity. DMD is characterized by progressive muscle weakness and a shortened life span, and there is no effective treatment. We used clustered regularly interspaced short palindromic repeat/Cas9 (CRISPR/Cas9)–mediated genome editing to correct the dystrophin gene (*Dmd*) mutation in the germ line of *mdx* mice, a model for DMD, and then monitored muscle structure and function. Genome editing produced genetically mosaic animals containing 2 to 100% correction of the *Dmd* gene. The degree of muscle phenotypic rescue in mosaic mice exceeded the efficiency of gene correction, likely reflecting an advantage of the corrected cells and their contribution to regenerating muscle. With the anticipated technological advances that will facilitate genome editing of postnatal somatic cells, this strategy may one day allow correction of disease-causing mutations in the muscle tissue of patients with DMD.

Duchenne muscular dystrophy (DMD) is caused by mutations in the gene for dystrophin on the X chromosome and affects approximately 1 in 3500 boys. Dystrophin is a large cytoskeletal structural protein essential for muscle cell membrane integrity. Without it, muscles degenerate, causing weakness and myopathy (*1*). Death of DMD patients usually occurs by age 25, typically from breathing complications and cardiomyopathy. Hence, therapy for DMD necessitates sustained rescue of skeletal, respiratory, and cardiac muscle structure and function. Although the genetic cause of DMD was identified nearly three decades ago (*2*), and several gene- and cell-based therapies have been developed to deliver functional *Dmd* alleles or dystrophin-like protein to diseased muscle tissue, numerous therapeutic challenges have been encountered, and no curative treatment exists (*3*).

RNA-guided, nuclease-mediated genome editing, based on type II CRISPR (clustered regularly interspaced short palindromic repeat)/Cas (CRISPR-associated) systems, offers a new approach to alter the genome (*4*–*6*). In brief, Cas9, a nuclease guided by single-guide RNA (sgRNA), binds to a targeted genomic locus next to the protospacer adjacent motif (PAM) and generates a double-strand break (DSB). The DSB is then repaired either by nonhomologous end-joining (NHEJ), which leads to insertion/deletion (indel) mutations, or by homology-directed repair (HDR), which requires an exogenous template and can generate a precise modification at a target locus (*7*). Unlike other gene therapy methods, which add a functional, or partially functional, copy of a gene to a patient's cells but retain the original dysfunctional copy of the gene, this system can remove the defect. Genetic correction using engineered nucleases (*8*–*12*) has been demonstrated in immortalized myoblasts derived from DMD patients in vitro (*9*), and rodent models of rare diseases (*13*), but not yet in animal models of relatively common and currently incurable diseases, such as DMD.

The objective of this study was to correct the genetic defect in the *Dmd* gene of *mdx* mice by CRISPR/Cas9–mediated genome editing in vivo. The *mdx* mouse (C57BL/10ScSn-*Dmd*^{mdx}/J) contains a nonsense mutation in exon 23 of the *Dmd* gene (*14*, *15*) (Fig. 1A). We injected Cas9, sgRNA, and HDR template into mouse zygotes to correct the disease-causing gene mutation in the germ line (*16*, *17*), a strategy that has the potential to correct the mutation in all cells of the body, including myogenic progenitors. Safety and efficacy of CRISPR/Cas9–based gene therapy was also evaluated.

[1]Department of Molecular Biology and Hamon Center for Regenerative Science and Medicine, University of Texas Southwestern Medical Center, Dallas, TX 75390, USA. [2]Department of Internal Medicine, University of Texas Southwestern Medical Center, Dallas, TX 75390, USA. *These authors contributed equally to this work. †To whom correspondence should be addressed. E-mail: eric.olson@utsouthwestern.edu

Initially, we tested the feasibility and optimized the conditions of CRISPR/Cas9–mediated *Dmd* gene editing in wild-type mice (C57BL6/C3H and C57BL/6) (see the supplementary materials). We designed a sgRNA to target *Dmd* exon 23 (fig. S1A) and a single-stranded oligodeoxynucleotide (ssODN) as a template for HDR-mediated gene repair (fig. S1B and table S1). The wild-type zygotes were co-injected with Cas9 mRNA, sgRNA-DMD, and ssODN and then implanted into pseudopregnant female mice. Polymerase chain reaction (PCR) products corresponding to *Dmd* exon 23 from progeny mice were sequenced (fig. S1, C to E). Efficiency of CRISPR/Cas9–mediated *Dmd* gene editing is shown in table S2.

We next applied the optimized CRISPR/Cas9–mediated genomic editing method to *mdx* mice (Fig. 1B). The CRISPR/Cas9–mediated genomic editing system will correct the point mutation in *mdx* mice during embryonic development via HDR or NHEJ (Fig. 1, C and D, and fig. S2A). "Corrected" *mdx* progeny (termed *mdx*-C) were identified by restriction fragment length polymorphism (RFLP) analysis and the mismatch-specific T7 endonuclease I (T7E1) assay (Fig. 1E, table S2, and supplementary materials). We analyzed a total of 11 different *mdx*-C mice. PCR products of *Dmd* exon 23 from seven *mdx*-C mice with HDR-mediated gene correction (termed *mdx*-C1 to C7) and four *mdx*-C mice containing NHEJ-mediated in-frame deletions of the stop codon (termed *mdx*-N1 to N4) were sequenced. Sequencing results revealed that CRISPR/Cas9–mediated germline editing produced genetically mosaic *mdx*-C mice displaying from 2 to 100% correction of the *Dmd* gene (Fig. 1E and fig. S2, B and C). A wide range of mosaicism occurs if CRISPR/Cas9–mediated repair occurs after the zygote stage, resulting in genomic editing in a subset of embryonic cells (*18*). All mouse progeny developed to adults without signs of tumor growth or other abnormal phenotypes.

We tested four different mouse groups for possible off-target effects of CRISPR/Cas9–mediated genome editing: (A) *mdx* mice without treatment (termed *mdx*), (B) CRISPR/Cas9–edited *mdx* mice (termed *mdx*+Cas9), (C) Wild-type control mice (C57BL6/C3H) without treatment (termed WT) and (D) CRISPR/Cas9–edited wild-type mice (termed WT+Cas9) (fig. S3A). Sequences of the target site (*Dmd* exon 23) and a total of 32 potential off-target (OT) sites in the mouse genome were predicted by the CRISPR design tool (http://crispr.mit.edu) and are listed in table S3. Ten of the 32 sites, termed OT-01 through OT-10, represent the genome-wide "top-10 hits." Twenty-two of the 32, termed OTE-01 through OTE-22 are located within exons.

Deep sequencing of PCR products corresponding to *Dmd* exon 23 revealed high ratios of HDR and NHEJ-mediated genetic modification in groups B and D but not in control groups A and C (fig. S3A and table S4). There was no difference in the frequency of indel mutations in the 32 potential off-target regions among the different groups (fig. S3, B and C, table S5, and supplementary materials). These results are also consistent with recent genome-wide studies showing that DNA cleavage by Cas9 is not promiscuous (*19*–*21*). Thus, off-target effects may be less of a concern in vivo than previously observed in vitro (*22*, *23*).

To analyze the effect of CRISPR/Cas9–mediated genomic editing on the development of muscular dystrophy, we performed histological analyses of four different muscle types [quadriceps, soleus (hindlimb muscle), diaphragm (respiratory muscle), and heart muscle] from wild-type mice, *mdx* mice, and three chosen *mdx-C* mice with different percentages of *Dmd* gene correction at 7 to 9 weeks of age. *mdx* muscle showed histopathologic hallmarks of muscular dystrophy, including variation in fiber diameter, centralized nuclei, degenerating fibers, necrotic fibers, and mineralized fibers, as well as interstitial fibrosis (Fig. 2 and figs. S4A and S5A). Immunohistochemistry showed no dystrophin expression in skeletal muscle or heart of *mdx* mice, whereas wild-type mice showed dystrophin expression in the subsarcolemmal region of the fibers and the heart (Fig. 2). Although *mdx* mice carry a stop mutation in the *Dmd* gene, we observed 0.2 to 0.6% revertant fibers, consistent with a previous report (*24*). *mdx*-C mice with 41% of the

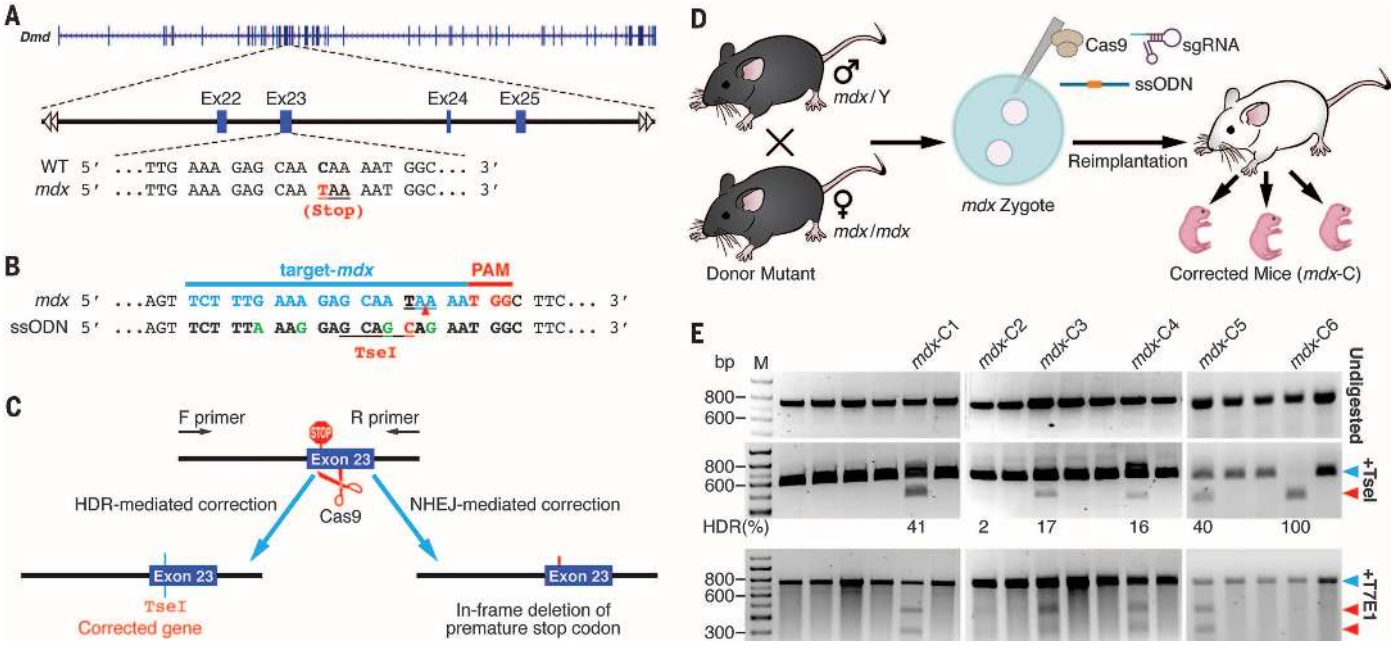

Fig. 1. CRISPR/Cas9–mediated *Dmd* correction in *mdx* mice. (**A**) Schematic of the targeted exon of mouse *Dmd* and sequence from wild-type (upper) and *mdx* mice (lower). The *mdx* point mutation (C to T) is marked in red, and the premature stop codon is underlined. (**B**) Schematic of the 20-nucleotide sgRNA target sequence of the *mdx* allele (blue) and the PAM (red). The red arrowhead indicates the Cas9 cleavage site. ssODN, which contains 90 base pairs (bp) of homology sequence flanking each side of the target site, was used as HDR template. ssODN incorporates four silent mutations (green) and adds a TseI restriction enzyme site (underlined) for genotyping and quantification of HDR-mediated gene editing (fig. S1B). (**C**) Schematic for the gene correction by HDR or NHEJ. The corresponding DNA and protein sequences are shown in fig. S2A. (**D**) Strategy of the gene correction in *mdx* mice via germline gene therapy. (**E**) Genotyping results of *mdx-C* mice with mosaicism of 2 to 100% corrected *Dmd* gene. Undigested PCR product (upper panel), TseI digestion (middle panel), and T7E1 digestion (lower panel) on a 2% agarose gel. The red arrowhead in the middle panel marks the DNA band indicating HDR-mediated correction generated by TseI digestion. The blue arrowhead marks the DNA band of the uncorrected *mdx* allele. The relative intensity of the DNA bands (indicated by blue and red arrowheads) reflects the percentage of HDR in the genomic DNA. The percentage of HDR is located under the middle panel. The band intensity was quantified by ImageJ (NIH). The blue and red arrowheads in the lower panel indicate uncut and cut bands by T7E1, respectively. M denotes size marker lane. bp indicates the length of the marker bands.

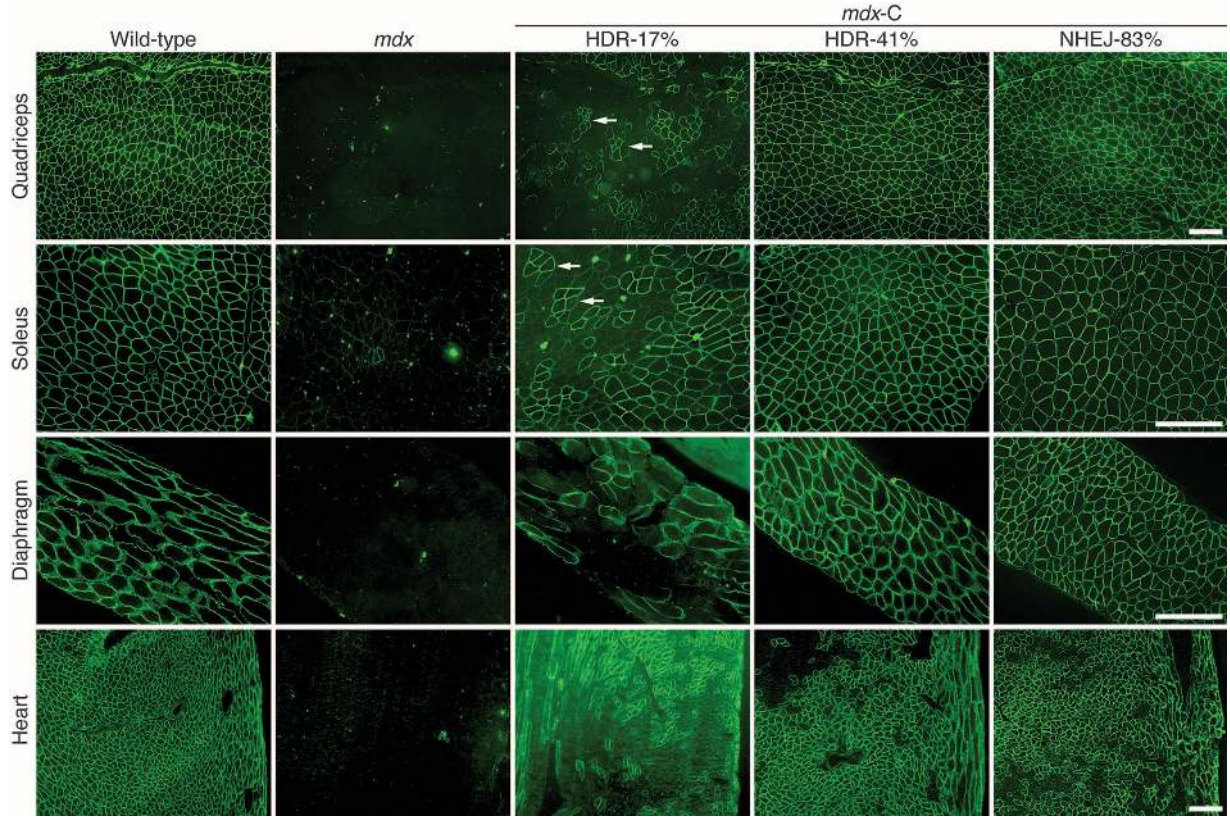

Fig. 2. Histological analysis of muscles from wild-type, *mdx*, and *mdx-C* mice. Immunostaining and histological analysis of muscles from 7- to 9-week-old wild-type, *mdx*, and *mdx*-C mice (HDR-17%, HDR-41%, or NHEJ-83%). Dystrophin immunofluorescence (green) in wild-type mice is present in all muscles, including quadriceps, soleus, diaphragm, and heart, and is absent in *mdx* mice, except for a single revertant fiber in skeletal muscle. Skeletal muscle from the HDR-17% mouse has a characteristic pattern of clusters of dystrophin-positive fibers adjacent to clusters of dystrophin-negative fibers, whereas HDR-41% or NHEJ-83% *mdx*-C skeletal muscle is composed of dystrophin-positive myofibers only. White arrows indicate the adjacent clusters of dystrophin-positive fibers. Scale bar, 100 μm.

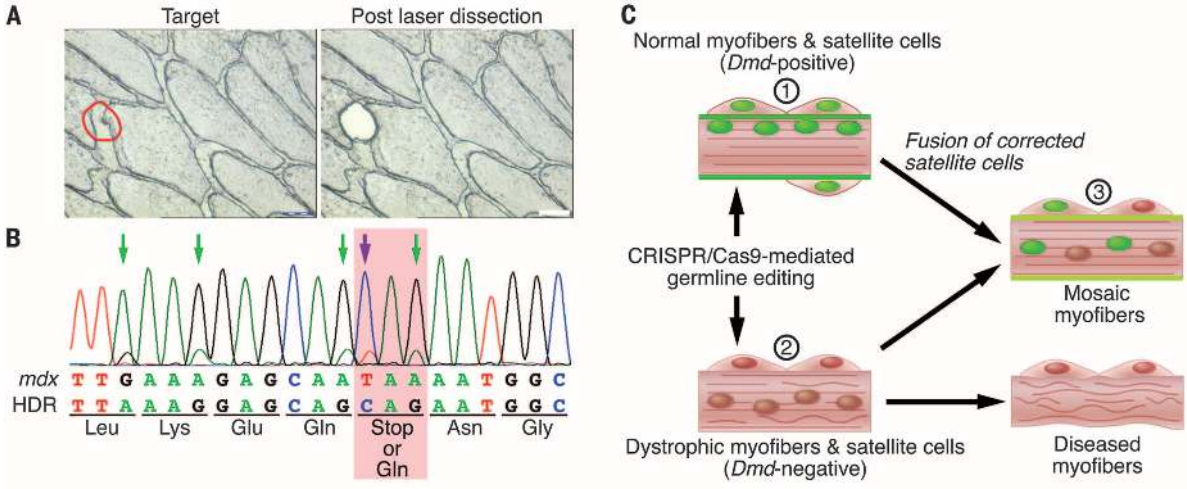

Fig. 3. Analysis of satellite cells from *mdx*-C mice and a model for rescue of muscular dystrophy by CRISPR/Cas9–mediated genomic correction. (**A**) Frozen sections of *mdx*-C gastrocnemius were mounted onto polyethylene membrane frame slides and immunohistochemically stained for Pax-7, a marker for satellite cells. Cross sections of muscle before (left) and after (right) laser dissection show the precise isolation of satellite cells (brown, in red circle). Scale bar, 25 μm. (**B**) PCR products corresponding to *Dmd* exon 23 were generated from genomic DNA isolated from satellite cells of *mdx*-C mice. PCR products were sequenced and show that CRISPR/Cas9–mediated genomic editing corrected a subset of satellite cells in vivo. Purple arrow indicates the corrected allele mediated by HDR. Green arrows indicate the silent mutation sites. The corresponding amino acid residues are shown under the DNA sequence. The red box indicates the corrected site. (**C**) A model for rescue of muscular dystrophy by CRISPR/Cas9–mediated genomic correction. There are three types of myofibers in *mdx*-C mice: (i) normal dystrophin-positive myofibers (green membrane) and satellite cells originating from corrected progenitors (green nuclei); (ii) dystrophic dystrophin-negative myofibers (brown membrane) and satellite cells originating from *mdx* progenitors (brown nuclei); and (iii) mosaic dystrophin-positive myofibers with centralized nuclei (green and brown nuclei) generated by fusion of corrected and *mdx* progenitors or by fusion of corrected satellite cells with preexisting dystrophic fibers. Immunostaining of the three types of myofibers in *mdx*-C mice is shown in fig. S8C.

Table 1. Serum creatine kinase (CK) levels and forelimb grip strength of wild-type, *mdx*, and *mdx*-C mice.

Litter	Mouse no.	Percent of correction	Sex	CK(U/L)	Forelimb grip strength (grams of force)					
					Trial 1	Trial 2	Trial 3	Trial 4	Trial 5	Avg. ± SD
No. 1	WT	–	M	318	170	163	140	132	169	154.8 ± 17.5
	mdx-04	0	M	6,366	64	56	52	59	57	57.6 ± 4.3
	mdx-06	0	M	7,118	102	123	109	79	97	102.0 ± 16.1
	***mdx*-C1**	**HDR-41%**	**M**	**350**	**141**	**150**	**154**	**143**	**133**	**144.2±8.1**
No. 2	WT	–	F	449	128	116	109	102	103	111.6 ± 10.7
	mdx-20	0	F	30,996	107	105	92	78	61	88.6 ± 19.3
	mdx-10	0	F	38,715	84	64	67	62	53	66.0 ± 11.3
	***mdx*-C3**	**HDR-17%**	**F**	**4,290**	**123**	**126**	**101**	**107**	**102**	**111.8±11.8**
No. 25	*mdx*-02	0	M	14,059	54	64	47	41	52	51.6 ± 12.1
	mdx-03	0	M	4,789	129	120	116	104	92	112.2 ± 35.6
	mdx-05	0	M	11,841	91	94	54	64	54	71.4 ± 24.0
	***mdx*-N1**	**NHEJ-83%**	**M**	**240**	**145**	**154**	**147**	**138**	**133**	**143.4±44.8**
	mdx-01	0	F	7,241	108	95	103	105	85	99.2 ± 30.5
	mdx-04	0	F	5,730	100	112	103	114	100	105.8 ± 32.3
	mdx-07	0	F	6,987	74	73	73	73	70	72.6 ± 19.6

mdx alleles corrected by HDR (termed HDR-41%) or with 83% correction by in-frame NHEJ (termed NHEJ-83%) showed complete absence of the dystrophic muscle phenotype and restoration of dystrophin expression in the subsarcolemmal region of all myofibers (Fig. 2). Strikingly, correction of only 17% of the mutant *Dmd* alleles (termed HDR-17%) was sufficient to allow dystrophin expression in a majority of myofibers at a level of intensity comparable to that of wild-type mice, and the muscle exhibited fewer histopathologic hallmarks of muscular dystrophy than *mdx* muscle (fig. S4A). The substantially higher percentage (47 to 60%) of dystrophin-positive fibers associated with only 17% gene correction (fig. S6, A and B) suggests a selective advantage of the corrected skeletal muscle cells. Western blot analysis showed restored dystrophin protein in skeletal muscle (quadriceps) and heart of *mdx*-C mice to levels consistent with percentages of dystrophin-positive fibers (figs. S4B and S6B).

To compare the efficiency of rescue over time, we chose *mdx-C* mice with comparable mosaicism of rescue of ~40%. As shown in fig. S7A, a 3-week-old *mdx*-C mouse with ~40% HDR-mediated gene correction (termed HDR-40%-3wks) showed occasional dystrophin-negative myofibers among a majority of dystrophin-positive fibers. In contrast, no dystrophin-negative fibers were seen in a mouse with comparable gene correction at 9 weeks of age, suggesting progressive rescue with age in skeletal muscle. In *mdx*-C mice with comparable mosaicism, we did not observe a significant difference in dystrophin expression in the heart between 3 and 9 weeks of age (fig. S7B), suggesting that age-dependent improvement may be restricted to skeletal muscle.

The widespread and progressive rescue of dystrophin expression in skeletal muscle might reflect the multinucleated structure of myofibers, such that a subset of nuclei with corrected *Dmd* genes can compensate for nuclei with *Dmd* mutations. Fusion of corrected satellite cells (the stem cell population of skeletal muscle) with dystrophic fibers might also progressively contribute to the regeneration of dystrophic muscle (*25*). To investigate this possibility, we identified satellite cells in muscle sections of *mdx*-C mice by immunostaining with Pax-7, a specific marker for satellite cells (fig. S8A). Using laser microdissection (see the supplementary materials), we dissected Pax-7 positive satellite cells and isolated genomic DNA for PCR analysis (Fig. 3A and fig. S8B). Sequencing results of PCR products corresponding to *Dmd* exon 23 from these isolated satellite cells showed the corrected *Dmd* gene (Fig. 3B). These results indicate that CRISPR/Cas9 genomic editing corrected the mutation in satellite cells allowing these muscle stem cells to rescue the dystrophic muscle (Fig. 3C and fig. S8C).

Serum creatine kinase (CK), a diagnostic marker for muscular dystrophy that reflects muscle leakage, was measured in wild-type, *mdx*, and *mdx*-C mice. Consistent with the histological results, serum CK levels of the *mdx*-C mice were substantially decreased compared with *mdx* mice and were inversely proportional to the percentage of genomic correction (Table 1). Wild-type, *mdx*, and *mdx*-C mice were also subjected to grip-strength testing to measure muscle performance, and the *mdx*-C mice showed enhanced muscle performance compared with *mdx* mice (Table 1).

Our results show that CRISPR/Cas9–mediated genomic editing is capable of correcting the primary genetic lesion responsible for muscular dystrophy (DMD) and preventing development of characteristic features of this disease in *mdx* mice. Because genome editing in the germ line produced genetically corrected animals with a wide range of mosaicism (2 to 100%), we were able to compare the percentage of genomic correction with the extent of rescue of normal muscle structure and function. We observed that only a subset of corrected cells in vivo is sufficient for complete phenotypic rescue. As schematized in Fig. 3C, histological analysis of partially corrected *mdx* mice revealed three types of myofibers: (i) normal dystrophin-positive myofibers; (ii) dystrophic dystrophin-negative myofibers; and (iii) mosaic dystrophin-positive myofibers containing centralized nuclei, indicative of muscle regeneration. We propose that the latter type of myofiber arises from the recruitment of corrected satellite cells into damaged myofibers, forming mosaic myofibers with centralized nuclei. Efforts to expand satellite cells ex vivo as a source of cells for in vivo engraftment have been hindered by the loss of proliferative potential and regenerative capacity of these cells in culture (*26*). Thus, direct editing of satellite cells in vivo by the CRISPR/Cas9 system represents a potentially promising alternative approach to promote muscle repair in DMD.

Genomic editing within the germ line is not currently feasible in humans. However, genomic editing could, in principle, be envisioned within postnatal cells in vivo if certain technical challenges could be overcome. For example, there is a need for appropriate somatic cell delivery systems capable of directing the components of the CRISPR/Cas9 system to dystrophic muscle or satellite cells in vivo. In this regard, the adeno-associated virus (AAV) delivery system has proven to be safe and effective and has already been advanced in clinical trials for gene therapy (*27*, *28*). Moreover, the AAV9 serotype has been shown to provide robust expression in skeletal muscle, heart, and brain, the major tissues affected in DMD patients. Other nonviral gene delivery methods, including injection of naked plasmid DNA (*29*), chemically modified mRNA (*30*, *31*), and nanoparticles containing nucleic acid (*32*), also warrant consideration. Another challenge with respect to the feasibility of clinical application of the CRISPR/Cas9 system is the increase in body size between rodents and humans, requiring substantial scale-up. More efficient genome editing in postnatal somatic tissues is also needed for the advancement of the CRISPR/Cas9 system into clinical use. Although CRISPR/Cas9 can effectively generate NHEJ-mediated indel mutations in somatic cells, HDR-mediated correction is relatively ineffective in postmitotic cells, such

as myofibers and cardiomyocytes, because these cells lack the proteins essential for homologous recombination (*33*). Coexpression of components of the HDR pathway with the CRISPR/Cas9 system might enhance HDR-mediated gene repair. Finally, safety issues of the CRISPR/Cas9 system, especially for long-term use, need to be evaluated in preclinical studies in large-animal models of disease. Despite the challenges listed above, with rapid technological advances of gene delivery systems and improvements to the CRISPR/Cas9 editing system (*33*), the approach we describe could ultimately offer therapeutic benefit to DMD and other human genetic diseases in the future.

REFERENCES AND NOTES

1. R. J. Fairclough, M. J. Wood, K. E. Davies, *Nat. Rev. Genet.* **14**, 373–378 (2013).
2. R. G. Worton, M. W. Thompson, *Annu. Rev. Genet.* **22**, 601–629 (1988).
3. J. C. van Deutekom, G. J. van Ommen, *Nat. Rev. Genet.* **4**, 774–783 (2003).
4. M. Jinek *et al.*, *Science* **337**, 816–821 (2012).
5. L. Cong *et al.*, *Science* **339**, 819–823 (2013).
6. P. Mali *et al.*, *Science* **339**, 823–826 (2013).
7. P. Mali, K. M. Esvelt, G. M. Church, *Nat. Methods* **10**, 957–963 (2013).
8. F. D. Urnov *et al.*, *Nature* **435**, 646–651 (2005).
9. D. G. Ousterout *et al.*, *Mol. Ther.* **21**, 1718–1726 (2013).
10. M. J. Osborn *et al.*, *Mol. Ther.* **21**, 1151–1159 (2013).
11. Y. Wu *et al.*, *Cell Stem Cell* **13**, 659–662 (2013).
12. G. Schwank *et al.*, *Cell Stem Cell* **13**, 653–658 (2013).
13. H. Yin *et al.*, *Nat. Biotechnol.* **32**, 551–553 (2014).
14. G. Bulfield, W. G. Siller, P. A. Wight, K. J. Moore, *Proc. Natl. Acad. Sci. U.S.A.* **81**, 1189–1192 (1984).
15. P. Sicinski *et al.*, *Science* **244**, 1578–1580 (1989).
16. H. Wang *et al.*, *Cell* **153**, 910–918 (2013).
17. H. Yang *et al.*, *Cell* **154**, 1370–1379 (2013).
18. S. T. Yen *et al.*, *Dev. Biol.* **393**, 3–9 (2014).
19. X. Wu *et al.*, *Nat. Biotechnol.* **32**, 670–676 (2014).
20. C. Kuscu, S. Arslan, R. Singh, J. Thorpe, M. Adli, *Nat. Biotechnol.* **32**, 677–683 (2014).
21. J. Duan *et al.*, *Cell Res.* **24**, 1009–1012 (2014).
22. V. Pattanayak *et al.*, *Nat. Biotechnol.* **31**, 839–843 (2013).
23. Y. Fu *et al.*, *Nat. Biotechnol.* **31**, 822–826 (2013).
24. S. R. Pigozzo *et al.*, *PLOS ONE* **8**, e72147 (2013).
25. H. Yin, F. Price, M. A. Rudnicki, *Physiol. Rev.* **93**, 23–67 (2013).
26. D. Montarras *et al.*, *Science* **309**, 2064–2067 (2005).
27. A. C. Nathwani *et al.*, *Mol. Ther.* **19**, 876–885 (2011).
28. M. A. Kotterman, D. V. Schaffer, *Nat. Rev. Genet.* **15**, 445–451 (2014).
29. B. Peng, Y. Zhao, H. Lu, W. Pang, Y. Xu, *Biochem. Biophys. Res. Commun.* **338**, 1490–1498 (2005).
30. M. S. Kormann *et al.*, *Nat. Biotechnol.* **29**, 154–157 (2011).
31. L. Zangi *et al.*, *Nat. Biotechnol.* **31**, 898–907 (2013).
32. T. J. Harris *et al.*, *Biomaterials* **31**, 998–1006 (2010).
33. P. D. Hsu, E. S. Lander, F. Zhang, *Cell* **157**, 1262–1278 (2014).

ACKNOWLEDGMENTS

We thank Z. Wang and B. Nelson for advice and constructive criticism; L. Sutherland, H. Zhou, and J. Ren for discussions and technical help; C. Xing and R. Kittler for analysis of off-target effects; S. Rovinsky and E. Plautz for grip-strength testing; and R. Hammer, J. Ritter, and J. Richardson for advice. We thank G. Church for hCas9 (human codon optimized Cas9) and the gRNA cloning vector plasmids. This work was supported by grants from NIH (HL-077439, HL-111665, HL-093039, DK-099653, and U01-HL-100401) and the Robert A. Welch Foundation (grant 1-0025 to E.N.O.).

SUPPLEMENTARY MATERIALS

www.sciencemag.org/content/345/6201/1184/suppl/DC1
Materials and Methods
Figs. S1 to S8
Tables S1 to S5
References (*34*–*37*)

7 April 2014; accepted 1 August 2014
Published online 14 August 2014;
10.1126/science.1254445

THE RIBOSOME

How the ribosome hands the A-site tRNA to the P site during EF-G–catalyzed translocation

Jie Zhou, Laura Lancaster, John Paul Donohue, Harry F. Noller*

Coupled translocation of messenger RNA and transfer RNA (tRNA) through the ribosome, a process catalyzed by elongation factor EF-G, is a crucial step in protein synthesis. The crystal structure of a bacterial translocation complex describes the binding states of two tRNAs trapped in mid-translocation. The deacylated P-site tRNA has moved into a partly translocated pe/E chimeric hybrid state. The anticodon stem-loop of the A-site tRNA is captured in transition toward the 30*S* P site, while its 3′ acceptor end contacts both the A and P loops of the 50*S* subunit, forming an ap/ap chimeric hybrid state. The structure shows how features of ribosomal RNA rearrange to hand off the A-site tRNA to the P site, revealing an active role for ribosomal RNA in the translocation process.

During the translocation step of the elongation phase of protein synthesis, the mRNA is advanced by one codon, coupled to movement of the tRNAs from the ribosomal A (aminoacyl) to P (peptidyl) and P to E (exit) sites, in a process catalyzed by elongation factor EF-G (*1*). First, the tRNAs move on the 50*S* subunit into P/E and A/P hybrid states, followed by movement of the tRNA anticodon stem-loops (ASLs) from the 30*S* subunit A and P sites to the P and E sites, respectively, coupled to movement of their associated mRNA codons (*2*). The first step is accompanied by intersubunit rotation (*3*–*7*), whereas the second step requires EF-G·guanosine triphosphate (GTP) and involves rotation of the 30*S* subunit head domain (*8*–*11*). Although much has recently been learned about the structural basis of P-tRNA movement to the E site (*9*, *10*, *12*, *13*), translocation intermediates containing A-tRNA are more difficult to trap. Thus, much of our thinking about the structural basis of A-tRNA and mRNA movement is based on crystal structures of EF-G bound to vacant (*14*) or P-tRNA–containing ribosome complexes trapped in classical (*15*) or hybrid states (*10*, *12*, *13*) and two cryogenic electron microscopy structures of 70*S* ribosome–EF-G complexes containing two tRNAs bound in P/E and A/P* hybrid states (*16*) or in ap/P and pe/E chimeric hybrid states (*11*). [We use lower-case letters to indicate that the tRNA is bound in a chimeric state within the small or large subunit, whereas upper-case letters indicate binding to the canonical A, P, or E sites of a subunit. For example, "pe/E" is meant to indicate that the ASL of the tRNA is bound between P-site elements of the small subunit head domain and E-site elements of the small subunit body, while its acceptor end is bound to the canonical E site of the large subunit.]

Center for Molecular Biology of RNA and Department of Molecular, Cell and Developmental Biology, University of California at Santa Cruz, Santa Cruz, CA 95064, USA.
***Corresponding author. E-mail: harry@nuvolari.ucsc.edu**

Here, we report the crystal structure of a 70*S* ribosome translocation intermediate containing EF-G, mRNA, and two tRNAs: a deacylated tRNA bound in the pe/E state and a peptidyl-tRNA trapped in an ap/ap chimeric hybrid state. The complex was formed with *Thermus thermophilus* 70*S* ribosomes, a 39-nucleotide mRNA, elongator $tRNA^{Met}$ in the P site, and *N*-acetyl-Val-$tRNA^{Val}$ in the A site. To trap the translocation intermediate, we added neomycin to block completion of translocation and fusidic acid to prevent release of EF-G (materials and methods and fig. S1). The structure was solved by using diffraction data to 3.8 Å obtained from a single crystal (table S1). Examples of electron density are shown in supplementary materials (figs. S2 to S13). Relative to the classical-state ribosome (*17*), the 30*S* subunit head undergoes a large 21° counterclockwise rotation, and the 30*S* body undergoes a 2.7° rotation relative to the 50*S* subunit (Figs. 1 and 2, A and B). The P-tRNA ASL moves with the 30*S* head into a position between the P site of the 30*S* head and the E site of the 30*S* body (pe chimeric state; Fig. 1, D and E), while its acceptor end moves fully into the 50*S* E site (Fig. 1C), forming a pe/E chimeric hybrid state (*9*–*11*). The A-tRNA ASL moves to within ~4 Å of the P-site elements of the 30*S* body (Fig. 1D); its elbow rotates toward the classical 50*S* P site, but its acceptor end is bound between the 50*S* subunit A and P sites (Fig. 1C), forming an ap/ap chimeric hybrid state. The large, EF-G–dependent rotation of the 30*S* head in our structure repositions helix H38 of 23*S* ribosomal RNA (rRNA), allowing the A-tRNA elbow to reach the position of the P-site tRNA elbow (fig. S14). Domain IV of EF-G is wedged into the site of convergence of the A-site mRNA codon, the anticodon loop of the ap/ap tRNA, and the 16*S* and 23*S* rRNAs at intersubunit bridge B2a, simultaneously contacting all four RNAs (fig. S15).

Although it is clear that 30*S* head rotation facilitates P-site ASL translocation (*9*–*11*), the A-site